Materials of Chemistry and Physics 122 (2010) 263-269

Preparation and structural characterization of SnO_2 and GeO_2 methanol steam reforming thin film model catalysts by (HR)TEM

H. Lorenz[1], Q. Zhao[1], S. Turner[2], O. I. Lebedev[2], G. Van Tendeloo[2], B. Klötzer[1], C. Rameshan[1,3], S. Penner[1,*]

[a]Laboratory of Industrial Chemistry, Ruhr University Bochum, D-44780 Bochum, Germany.
[b]Institute of Geology, Mineralogy & Geophysics, Ruhr-University Bochum, D-44780 Bochum, Germany
[c]Fritz-Haber-Institut der Max-Planck-Gesellschaft, Departement of Inorganic Chemistry, D-14195 Berlin, Germany

* Corresponding author: e-mail simon.penner@uibk.ac.at,

Received 21 October 2009; revised 23 December 2009; accepted 23 March 2010. Available online 17 April 2010.

Abstract

Structure, morphology and composition of different tin oxide and germanium oxide thin film catalysts for the methanol steam reforming (MSR) reaction have been studied by a combination of (High-resolution) Transmission Electron Microscopy, Selected Area Electron Diffraction, Dark-field imaging and Electron Energy-Loss Spectroscopy. Deposition of the thin films on NaCl(001) cleavage faces has been carried out by thermal evaporation of the respective SnO_2 and GeO_2 powders in varying oxygen partial pressures and at different substrate temperatures. Preparation of tin oxide films in high oxygen pressures (10^{-3} mbar) exclusively resulted in SnO phases, at and above 473 K substrate temperature epitaxial growth of SnO on NaCl(001) leads to well-ordered films. For lower oxygen partial pressures (10^{-4}-10^{-5} mbar), mixtures of SnO and β-Sn are obtained. Well-ordered SnO_2 films, as verified by electron diffraction patterns and energy loss spectra, are only obtained after post-oxidation of SnO films at temperatures $T \geq 673$ K in 1 bar O_2. Preparation of GeO_x films inevitably results in amorphous films with a composition close to GeO_2, which cannot be crystallized by annealing treatments in oxygen or hydrogen at temperatures comparable to SnO/SnO_2. Similarities and differences to neighbouring oxides relevant for selective MSR in the third group of the periodic system (In_2O_3 and Ga_2O_3) are also discussed with the aim of cross-correlation in formation of nanomaterials, and ultimately, also catalytic properties.

Keywords: Electron Microscopy, Electron-Energy Loss Spectroscopy, SnO, Thin Films, Catalysis

1. Introduction

SnO_2 is one of the most extensively studied and best characterized oxides thanks to its outstanding chemical and electronic properties. A comprehensive review of all aspects especially of its surface and materials science has been given by Batzill et al.[1]. Recent important applications of SnO_2 range from solid state gas sensors (especially for reducing gases such as H_2, CO or H_2S) over transparent conductors to heterogeneous catalysis [1,2]. As these applications strongly depend on the structure and morphology of the SnO_2 samples, special attention has been paid to the development of reproducible preparation methods of a variety of SnO_2 samples, especially ordered thin films suitable for (high-resolution) transmission electron microscopy HR(TEM) characterization. These methods include sputtering, spray pyrolysis, electron-beam evaporation, chemical vapour deposition or rheotaxial growth and thermal oxidation, among others [3-7]. A concise discussion of different preparation techniques for thin films has been outlined by Sberveglieri et al.[8]. Regarding heterogeneous catalysis, the activity and selectivity of SnO_2 catalysts can be significantly improved by doping with other metals, such as Cu, Pd, Cr or Sb, but even pure SnO_2 itself is an active oxidation catalyst, especially in CO oxidation reactions. Since a Mars-van-Krevelen-type reaction mechanism is assumed to be prevalent, a central issue in oxidation catalysis of SnO_2 refers to its easy (surface) reducibility [1]. Most important, recent investigations indicate that pure SnO_2 exhibits a pronounced activity and/or selectivity in methanol steam

reforming [9]. This behaviour places SnO_2 in line with other, previously studied oxides such as ZnO [10], Ga_2O_3 [11] or In_2O_3 [12]. The main feature of all these oxides is their role as supports and/or catalysts in methanol steam reforming, but, depending on the surface chemistry and redox properties, the desired selectivity to CO_2 varies. Pure In_2O_3 is highly CO_2-selective, both ZnO and Ga_2O_3 are not [11,13]. Partly this is also due to their activity in the reverse water-gas shift reaction [14,15]. From a chemical analogy argument, Sn^{4+} and In^{3+} represent isoelectronic species and therefore we may speculate about a potential functional analogy of their catalytic action. The same holds for Ge^{4+}, Ga^{3+} and Zn^{2+}, which renders an extension of the studies to the fourth main group of the periodic system useful. Contrary to SnO_2, structural information on GeO_2 thin films is scarce and mainly limited to the preparation of GeO_2 nanomaterials [16-18]. Catalytic information on GeO_2 is virtually non-existent, especially concerning methanol steam reforming.

In order to close the materials gap between surface studies especially on tin oxides, where a considerable amount of data already exists [1] and studies on "real world" powder catalysts, the thin film model concept will be exploited. From the structural point of view, thin films grown on well-ordered substrates are usually epitaxial or at least well-ordered, that is, structurally resembling single crystal studies conducted in UHV. At the same time, our thin film dedicated micro reactor setup allows correlation of the catalytic activity/selectivity measured on both thin film and powder samples [11,12]. The aim of the present contribution therefore is - in close correlation to similar studies on Ga_2O_3 and In_2O_3 [11,12] - to use NaCl(001) cleavage faces as substrates to eventually grow single-crystalline tin and germanium oxide films to present an easy and reproducible preparation pathway to different thin film model systems of tin and germanium oxides and subsequently their thorough structural characterization, prior to catalytic testing (see part B [19]). Adequate tools to fulfil this task are considered HRTEM, selected area electron diffraction (SAED) and electron energy-loss spectroscopy (EELS). In part B [19] the structural properties are linked to catalytic activity and selectivity in methanol steam reforming. Special attention will also be paid to the influence of deposition parameters (O_2 background pressure, substrate temperature) on film stoichiometry and morphology.

2. Experimental

All tin and germanium oxide films were prepared in a high-vacuum chamber operated at a base pressure of 10^{-4} Pa. Film thicknesses (usually 25nm) were measured in-situ by a quartz crystal microbalance. SnO_2 and GeO_2 powders (Tin (IV) oxide, 99.99%, and Germanium (IV) oxide, 99.9999%, both Alfa Aesar) were thermally evaporated from tantalum crucibles onto vacuum-cleaved NaCl (001) surfaces at varying substrate temperatures (298 K-603 K) and O_2 background pressures (10^{-5}-10^{-3} mbar). The films were floated and rinsed with distilled water, dried and finally mounted on gold grids for electron microscopy. Annealing and oxidative treatments (1 bar He or O_2 for 1 h at 473 K, respectively) were performed in a circulating batch reactor. The structure and morphology of these thin films in the as-deposited state and upon oxidative and annealing treatments were monitored by (High-resolution)-Transmission Electron Microscopy (HRTEM). The electron diffraction patterns were externally calibrated with respect to the (111), (200) and (220) Pd reflections of an as-deposited, untreated Pd/Ga_2O_3 catalyst. Overview TEM imaging and Selected Area Electron Diffraction (SAED) were carried out with a ZEISS EM10C microscope, high-resolution imaging, Electron Energy-Loss Spectroscopy (EELS), and Dark-Field imaging were performed using a JEOL 4000EX high resolution microscope operated at 400 kV and a JEOL 3000F FASTEM microscope operated at 300 kV and equipped with a GIF 2000 post-column electron energy-loss spectrometer. The film composition was checked by Energy-dispersive X-ray Analysis (EDXS), which only showed peaks due the evaporated elemental thin film constituents (Sn, Ge and O) and the gold grid (Au). Surface carbon impurities present on the films were removed by Ar-sputtering prior to TEM imaging. The purity of the substrate was ensured by freshly cleaving the NaCl(001) crystals immediately before deposition of the oxide.

3. Results and Discussion

3.1. SnO and SnO_2 thin films

3.1.1. Preparation of SnO thin film model catalysts

The structure of the SnO films after deposition in 10^{-3} mbar Pa O_2 at low substrate temperatures (373 K) is shown in Figure 1. Although the film exhibits no pronounced contrast in bright-field TEM images, its regular grain-size structure is easily visible. The average size of the round-shaped grains is approximately 10 nm. The corresponding SAED pattern (shown as inset) represents an almost amorphous structure and shows a single blurred diffraction ring. Raising the substrate temperature to 473 K converts the film into a single crystalline phase, as revealed by the SAED pattern shown in Figure 2b. Four-fold split intense diffraction spots at 2.7Å, 1.9Å and 1.3Å correspond to the SnO (110), (200) and (220) lattice spacings of the tetragonal SnO phase (lattice constants a=3.79Å and c=4.84Å respectively [d_{theor}(110) = 2.686Å, d_{theor}(200) = 1.899Å, d_{theor}(220) = 1.343Å] [20]. As expected for the tetragonal phase, the (110)/(2-20) spots form an angle of 45° with the (200) diffraction spots. The corresponding bright-field TEM image (Figure 2a) exhibits much enhanced diffraction contrast and shows extended dark domains corresponding to differently oriented SnO grains. These observations are corroborated by additional high-

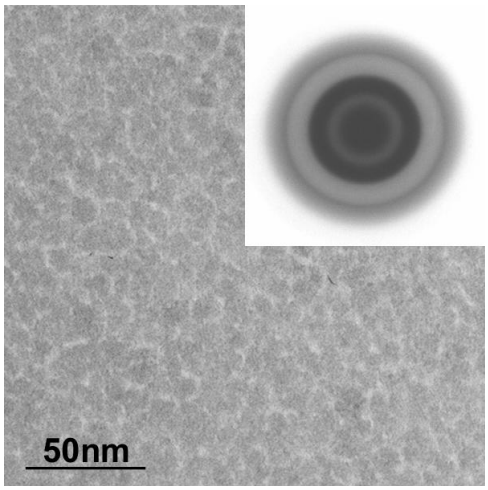

Fig. 1: Overview bright-field TEM image of a SnO thin film after deposition at 373 K on NaCl(001) in 10^{-3} mbar O_2. The SAED pattern is shown as an inset.

resolution imaging, shown in Figure 3. The HRTEM image in Figure 3 reveals a complex arrangement of individual SnO grains each exhibiting lattice fringes of ~ 3.0Å, corresponding to the SnO (101) lattice spacings [d_{theor}(101)=2.989Å] [20]. The inset Fast Fourier Transform pattern (i.e. the micro-diffraction pattern) evidences these extended SnO(101) lattice spacings by an ring at ~ 3.0Å, in agreement with the SAED patterns obtained from this sample. The FFT pattern also shows some reflections at ~ 2.7 Å spacing, corresponding to the SnO (110) lattice spacing. Both electron diffraction and HRTEM therefore unambiguously confirm that after deposition at 473 K in 0.1 Pa O_2 a single, well-ordered SnO phase is formed. Furthermore, the SAED pattern of Figure 2b suggests a preferential epitaxial growth of SnO on NaCl(001) in the relationship SnO[001]//NaCl[001] and SnO[011]//NaCl[011]. These observations agree well with previous studies of Choi et al. or Feng et al., where highly oriented tin oxide films (mostly tetragonal SnO_2) were successfully grown on single

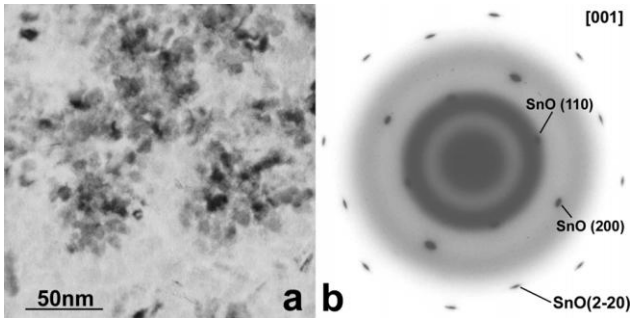

Fig. 2: Overview bright-field TEM image of a SnO thin film after deposition at 473 K on NaCl(001) in 10^{-3} mbar O_2 (a). The SAED pattern (b) evidences the tetragonal SnO crystal structure of the film.

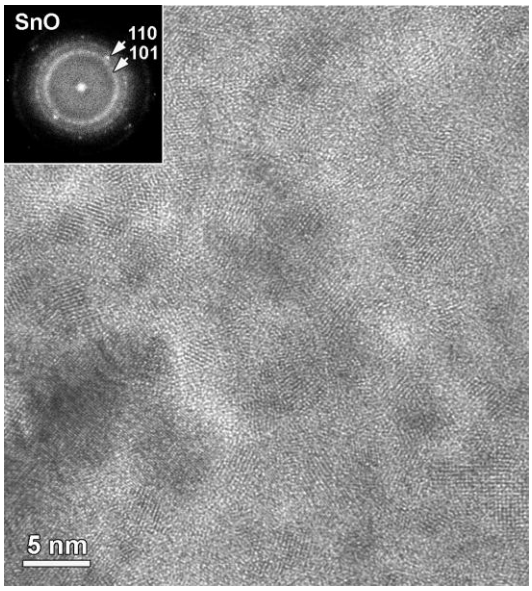

Fig. 3: High-resolution electron micrograph of the SnO thin film shown in Figure 2. The inset FFT pattern shows a strong ring corresponding to the 3.0Å {101} spacing of tetragonal SnO. A single reflection corresponding to the 2.7 Å {110} spacing is also present.

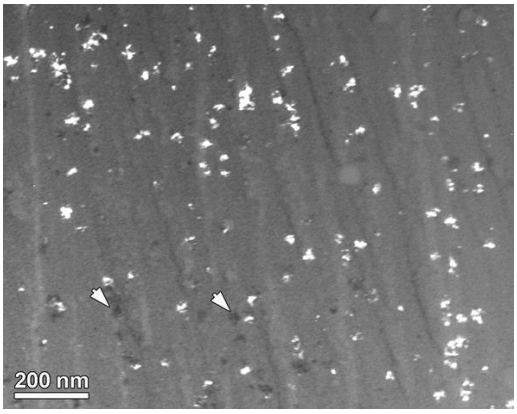

Fig. 4: Dark-field image of the SnO film shown in Figure 2 obtained using the SnO(200) diffraction reflection. The bright regions correspond to grains giving rise to the 200 reflection. Other differently oriented grains remain dark (examples indicated by arrows).

crystalline Al_2O_3 substrates [2,21]. From dark-field experiments (shown in Figure 4) we also infer that the contrast variations are due to diffraction contrast of differently oriented SnO grains. The dark-field image was taken by using the SnO (200) diffraction spot. Consequently, grains giving rise to this diffraction spot appear bright in the dark-field image. All other differently oriented grains remain dark (see e.g. areas indicated by arrows in the lower left corner of the image).

A more complex scenario is present if the substrate temperature is raised to 573 K (Figure 5). The bright-field TEM image in Figure 5a shows a complete reconstruction of the SnO structure and extended Moire-fringes indicate overlapping lattice of differently oriented SnO grains. However, the SAED patterns (not shown) are identical to

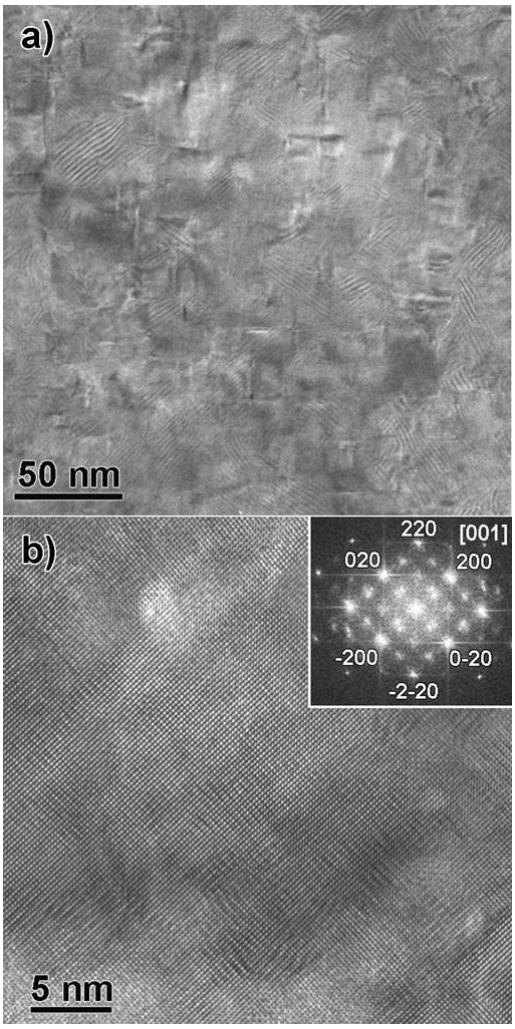

Fig. 5: Overview bright-field TEM image of a SnO thin film after deposition at 573 K on NaCl(001) in 10^{-3} mbar O_2 (a) and a HRTEM image showing a small SnO_2 region within the SnO film (b). The [001] zone axis orientation and structure of the SnO_2 region is evidenced by the inset FFT pattern.

the one shown in Figure 2b, indicating that most of the film remains SnO. Some small areas of the film have however almost fully oxidised to SnO_2 as a result of the raising of the substrate temperature. The high-resolution image image in Figure 5b shows such an area. All reflections in the FFT pattern fit with the tetragonal SnO_2 structure imaged along the [001] zone axis orientation.

The effect of O_2 background pressure variation at constant substrate temperature is highlighted in Figure 6. The left panel shows growth of SnO at 473 K in 10^{-4} mbar O_2, on the right panel the same situation in 10^{-5} mbar O_2 is outlined. In the TEM image of Figure 6a the former SnO structure formed after deposition at 473 K in 10^{-3} mbar O_2 is still prevailing, but additional round-shaped grains of about 20-30 nm size are also observed. The SAED pattern (inset) still shows strong diffraction spots of the tetragonal SnO phase, but also additional Debye-Scherrer-type diffraction rings. A detailed analysis reveals the presence of a second metallic β-Sn phase, with strong reflections at 2.9Å

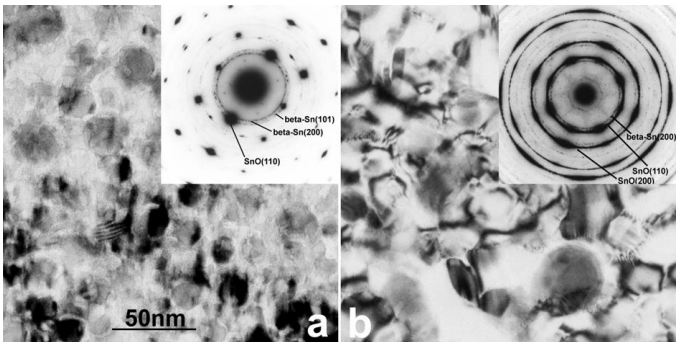

Fig. 6: Overview bright-field TEM image of a SnO thin film after deposition at 473 K on NaCl(001) in 10^{-4} mbar O_2 (a) and 10^{-5} mbar O_2 (b). The SAED patterns are shown as insets.

and 2.8Å, corresponding to the β-Sn(200) and β-Sn(101) fringes [d_{theor}(200)=2.915 Å and d_{theor}(101)=2.792 Å] [22]. It is worth noting, that these sphere-like structure corresponds to the first stages of oxide film preparation by rheotaxial growth and thermal oxidation [7,8], where metallic tin is deposited to form large droplets and subsequently oxidized to result in an oxide film with a high surface-to-volume ratio. These features are even more pronounced if the deposition is carried out with less O_2 (Figure 6b). At 10^{-5} mbar O_2 background pressure the film structure does not resemble SnO, but rather shows very large sphere-like aggregates (up to 50 nm in size). The SAED patterns still show SnO, but the intensity of the β-Sn phase increased considerably.

The issue of influence of O_2 background pressure on phase formation has also been addressed by Jimenez et al. upon SnO and SnO_2 deposition on MgO and SiO_2 [23]. In agreement with the present studies, heating of SnO_2 and post-exposition to 0.1 Torr (~13 Pa) O_2 for 300 s resulted only in SnO stoichiometry. Complete oxidation to SnO_2 was only obtained after exposure to an oxygen plasma at 300 K. In general, SnO thin films are mostly prepared via oxidation of Sn layers [24] or spray pyrolysis [25]. However, the above-outlined preparation method is unique since it yields reproducible and well-ordered SnO films at low substrate temperatures.

3.1.1. Preparation of SnO_2 thin film model catalysts

The question how to reproducibly prepare SnO_2 thin films is intimately connected with the ability to carry out deposition of tin oxides at oxygen background pressures higher than 10^{-3} mbar. Usually, e.g. for Ga_2O_3 or In_2O_3, an oxygen background pressure of 10^{-4} mbar is sufficient to fully oxidize the respective thin films during deposition. Deposition of tin oxides is different since both of the oxides, SnO and SnO_2, are thermodynamically stable oxides and deposition in 10^{-3} mbar O_2 only leads to SnO phases. Higher oxygen background pressures, even if they are needed for SnO_2 deposition, are basically excluded since the deposition rate decreases drastically for very high oxy

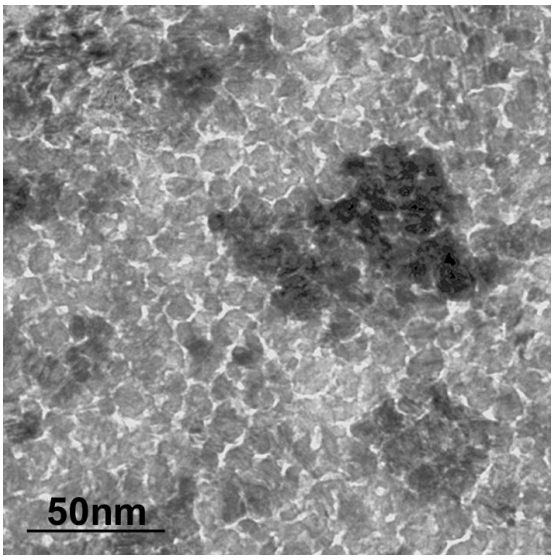

Fig. 7: Overview bright-field TEM image of a SnO thin film after deposition at 573 K on NaCl(001) in 10^{-3} mbar O_2 after post-oxidation at 673 K in 1 bar O_2 for 1h.

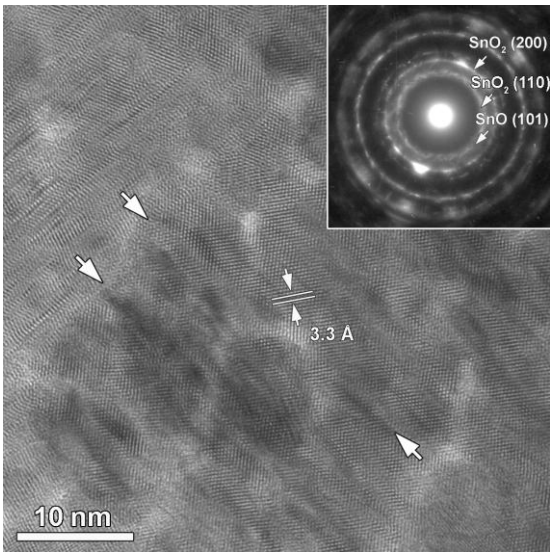

Fig. 8: High-resolution electron micrograph of the thin film shown in Figure 7. The inset SAED pattern evidences the tetragonal SnO_2 crystal structure, a faint diffuse ring corresponding to the SnO (101) spacing can also be made out. The arrows indicate examples of widespread defects (stacking faults) present in the film.

gen background pressures due to oxidative inhibition of the formation of volatile gas phase species. Hence, the only preparation pathway to SnO_2 thin films, if the deposition is carried out by thermal evaporation of SnO_2 is via formation of SnO and adequate post-oxidation procedures.

Figure 7 highlights the structure of a previous SnO film prepared at 473 K in 10^{-3} mbar oxygen background pressure and post-oxidized at 673 K in 1 bar O_2. The overview TEM image reveals a coarse grain structure similar to the original SnO film and exhibits strong diffraction contrast. However, the corresponding HRTEM images and SAED patterns indicate formation of SnO_2. Figure 8 shows a high-resolution TEM image with extended SnO_2(110) lattice fringes of 3.30Å spacing, corroborating the SAED analysis. The inset ED ring pattern mainly shows rings corresponding to the SnO_2 structure (at 3.4Å, 2.6 Å, 2.4 Å and 1.8 Å, corresponding to the (110), (101), (200) and (211) reflections of the tetragonal SnO_2 structure (a=4.73Å, c=3.18Å; d_{theor}(110)=3.347Å; d_{theor}(101)=2.643Å; d_{theor}(200)=2.369Å; d_{theor}(211)=1.764Å] [26]). It is worth noting, that SnO_2 appears to be at least partially ordered, as judged from the elongated diffraction spots overlapping with the diffraction rings. A single diffuse ring at 3.0 Å is present, arising from a very small amount of SnO. The arrows in the HRTEM image indicate the wide spread defective (mainly stacking faults) structure of the SnO_2 film. Additional information on the formation of different tin oxide species is provided by EELS. Figure 9 shows an overview of the Sn $M_{4,5}$ and O-K edges of SnO films after deposition at 473 K in 10^{-3} mbar O_2 (middle), after post-oxidation at 673 K (top) and after reduction at 573 K in 1 bar hydrogen (bottom). The interaction of the tin oxides with hydrogen is discussed in part B, but for the sake of clarity, the EELS spectrum is included in this figure. Due to the different structural environments in SnO and SnO_2 (tetrahedral vs. trigonal oxygen coordination in the first coordination shell) [27] the electron-energy near-edge structure of the Sn $M_{4,5}$ and O K-edges is a reliable tool to distinguish between the different types of tin oxides. The topmost spectrum is typical for SnO_2, with a wider splitting of the peaks in the region 530-550 eV and the more pronounced multiple scattering resonances at higher energy

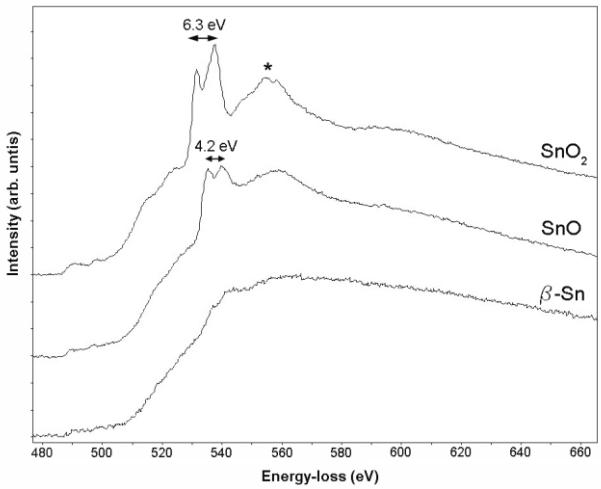

Fig. 9: EELS spectra (Sn-$M_{4,5}$ edge at 485 eV and O-K edge at 532 eV) of differently prepared tin oxide thin films (top: SnO_2 corresponding to the thin film shown in Figure 7; middle: SnO corresponding to the film shown in Figure 2; bottom: SnO thin film after reduction in H_2 at 573 K (1 bar, 1h). The two oxide phases can be discerned by the splitting of the fine structure after 530 eV as well as the elevated peak at 550-560 eV in SnO_2 (indicated by *) [27]

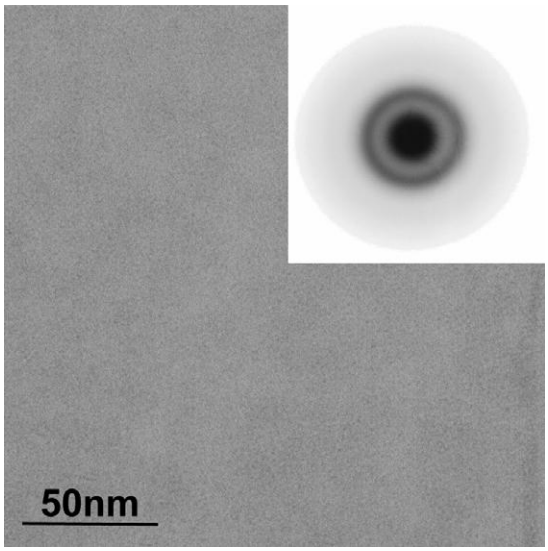

Fig. 10: Overview bright-field TEM image of a GeO_2 thin film after deposition at 300 K in 10^{-4} mbar O_2. The SAED pattern is shown as an inset.

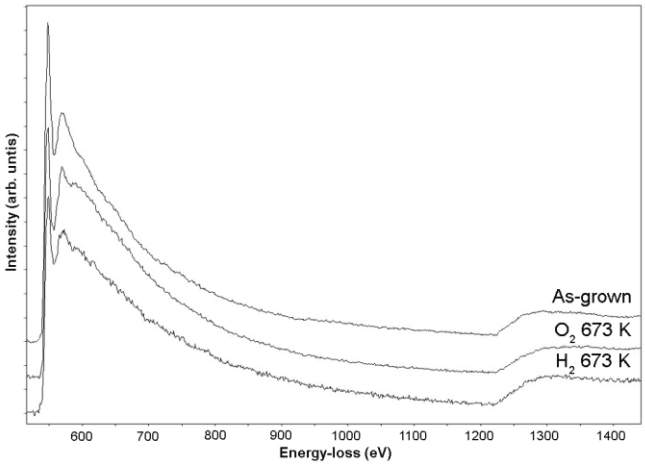

Fig. 11: EELS spectra (O-K edge at 532 eV and Ge $L_{2,3}$ at 1217 eV) of differently prepared germanium oxide thin films (top: GeO_2 corresponding to the thin film shown in Figure 10; middle: GeO_2 film after oxidation in O_2 at 673 K (1 bar, 1h); bottom: GeO_2 thin film after reduction in H_2 at 673 K (1 bar, 1h).

losses (around 575 eV). In contrast, the middle spectrum shows two peaks of almost equal intensity with a narrower splitting and a slightly less pronounced ELNES around 570-575 eV. These differences are basically due to the different coordination of oxygen in both tin oxides [27]. The bottom spectrum, corresponding to β-Sn according to the SAED patterns, only shows a broad edge typical for a delayed Sn $M_{4,5}$ edge [27].

3.2. GeO_2 thin films

The preparation of ordered, single-phase GeO_2 thin films is hampered by the polymorphism of GeO_2, that is, it exists not only a hexagonal α-quartz-type and a tetragonal rutile-type structure but also a glassy amorphous phase depending on pressure, temperature and preparation conditions. Concerning the preparation of thin films using NaCl as growth templates, the solubility of the different polymorphs in water is most crucial. Whereas α-quartz-type GeO_2 is slightly soluble in water, rutile-type GeO_2 is insoluble [28]. Depending on which phase forms, floating the thin films in water therefore might pose problems, as was the case for ZnO [29]. However, as discussed below, we succeeded in preparing self-supporting GeO_2 films, which are not affected by the floating procedure. Generally, GeO_2 samples are almost uniquely prepared by oxidative treatments of Ge films or powders [18,30].

For GeO_2 we followed a similar strategy as for SnO and SnO_2 and tried to assess structure, composition and influence of deposition parameters. Figure 10 shows a bright-field overview TEM image of a GeO_2 thin film prepared at 300 K and 10^{-4} mbar O_2 background pressure. Both the image and the SAED pattern (inset) indicate the presence of an amorphous germanium oxide phase. It is worth to note, that neither raising the substrate temperature to 623 K nor post-oxidation treatments up to 673 K lead to the formation of single crystalline phases and only low contrast amorphous structures are obtained. Recent studies have shown that thin films prepared by evaporation of GeO_2 are usually sub-stoichiometric and can only be crystallized by post-annealing at very high temperatures [31,32]. Our observations agree well with studies of Ardyanin et al. on the structure and photoluminescence properties of e-beam evaporated GeO_x films. GeO_2 was evaporated in UHV at 10^{-8} Torr (with pressure increase to $3x10^{-6}$ Torr during deposition) at 373 K on silicon substrates and only amorphous GeO_x films were obtained (film thickness: 200 nm). Only after annealing at 773 K, disproportion of GeO_x into crystalline Ge metal and amorphous GeO_2 was observed [32]. As the method of choice to gain information on the composition of the amorphous GeO_2 films, EELS spectra of the as-deposited thin film, after oxidation at 673 K and after reduction in hydrogen at 673 K were collected. This will also ensure a direct correlation to the properties of SnO_x films. Figure 11 highlights a set of O K-edges and Ge $L_{2,3}$-edges of the films after the above mentioned treatments. In short, these edges are typical of α-quartz-type GeO_2 [33] and no substantial differences between the spectra can be detected. Most important, the spectra allow the determination of the film stoichiometry by quantification of the oxygen-to-germanium ratios. For the as-deposited film and the oxidized sample, ratios of O : Ge = 66 at% : 34 at% and 67 at % : 33 at%, respectively, have been obtained. This indicates that already after deposition the film stoichiometry is close to GeO_2. For the reduced sample, this ratio shifts to O : Ge = 58 at% : 42 at%, indicating that the overall film stoichiometry changes towards GeO.

We therefore assume that the films are close to a GeO_2 stoichiometry in the as-deposited state and annealing treatments (also in hydrogen and oxygen) up to 673 K, which

are typically used for catalyst regeneration treatments, are not sufficient to induce a complete reduction of GeO_2, disproportion of GeO_x or the formation of any crystalline phase (metallic or oxidic).

4. Conclusions

We successfully demonstrated reproducible preparation pathways to thin film model catalysts of SnO, SnO_2 and GeO_2 by simple thermal evaporation of SnO_2 and GeO_2 in different oxygen environments and, for SnO_2, by post-oxidation of the resulting films at 673 K. Generally, some differences and similarities to the previously studied neighbouring oxides (In_2O_3, Ga_2O_3) in the third group of the periodic system are notable [11,12]. From the structural point of view, SnO/SnO_2 more closely resembles In_2O_3 thin films in terms of crystallinity and epitaxial growth. Both materials show a strong dependence of the film structure and morphology on the substrate temperature, although formation of nano-materials, such as octahedrons or pyramidal-shaped particles as obtained for In_2O_3, has never been observed. On the contrary, GeO_2 films resemble Ga_2O_3 structures, at least at low substrate temperatures. For both materials, amorphous structures are usually observed, even after oxidative and annealing treatments at temperatures as high as 673 K. As for SnO/SnO_2, no nano-architectures have been observed for GeO_2 even at high substrate temperatures (623 K). This behaviour might be interpreted in terms of the presence of different growth species during oxide deposition and the resulting altered wetting properties on NaCl(001). For Ga_2O_3 and In_2O_3, these growth species were basically associated with sub-stoichiometric oxides (e.g. Ga_2O or In_2O) with a high mobility on NaCl(001) at high substrate temperatures. Therefore, the formation of the sphere-like aggregates for Ga_2O_3 and pyramidal-shaped particles for In_2O_3 is the result of efficient transport processes preceding the oxidation of the volatile sub-stoichiometric oxides and their re-oxidation towards ordered aggregates (apart from crystallographic matching of In_2O_3 and NaCl)). For SnO_2 we might interpret the growth species as SnO and/or Sn metal, as confirmed by the SAED patterns of films prepared at different oxygen partial pressures. The highest oxygen partial pressures that can be used in our HV chamber during deposition (10^{-3} mbar) are sufficient to convert Sn metal into SnO, but no further oxidation to SnO_2 can be achieved. The same probably holds for GeO_2, but since only amorphous films are obtained, a thorough structural characterization by TEM, apart from EELS, is excluded. In any case, both oxides are promising candidates as supports for small Pd catalyst particles. Hence, bimetallic single phases of Pd-Sn and Pd-Ge might be prepared by reduction in hydrogen and catalytically characterized in methanol steam reforming, in close correlation to Pd supported on ZnO, Ga_2O_3 and In_2O_3.

Acknowledgements

We thank the FWF (Austrian Science Foundation) for financial support under project P20892-N19. The authors acknowledge support from the European Union under the Framework 6 program under a contract from an Integrated Infrastructure Initiative (Reference 026019 ESTEEM).

References

[1] M. Batzill, U. Diebold, Prog. Surf. Sci. 79 (2005) 47-154
[2] Y. Choi, S. Hong, Sens. Actuators B 125 (2007) 504-509
[3] S. Semancik, R. Cavicchi, Thin Solid Films 206 (1991) 81-87
[4] K. Murakami, K. Nakajima, S. Kaneko, Thin Solid films 515 (2007) 8632-8636
[5] C. F. Wan, R. D. McGrath, W. F. Keenan, S. N. Frank, J. Electrochem. Soc. 136 (1989) 1459-1463
[6] Q. Wu, J. Song, J. Kang, Q. Dong, S. Wu, S. Sun, Mater. Lett. 61 (2007) 3679-3684
[7] G. Sberveglieri, G. Faglia, S. Gropelli, P. Nelli, Proc. 6th Int. Conf. Solid-State Sensors and Actuators, San Francisco, CA, USA, June 23-27, 1991, p. 165-168
[8] G. Sberveglieri, Sens. Actuators B 6 (1992) 239-247
[9] T. Mori, S. Hoshino, A. Neramittagapong, J. Kubo, Y. Morikawa, Chem Lett. 13 (2002) 390-391
[10] [10] C. Wöll, Prog. Surf. Sci 82 (2007) 55-120
[11] S. Penner, H. Lorenz, W. Jochum, M. Stöger-Pollach, D. Wang, C. Rameshan, B. Klötzer, Appl. Catal. A 358 (2009) 193-202 and references therein
[12] H. Lorenz, W. Jochum, B. Klötzer, M. Stöger-Pollach, S. Schwarz, K. Pfaller, S. Penner,Appl. Catal. A 347 (2008) 34-42 and references therein
[13] A. Neramittagapong, S. Hoshino, T. Mori, J. Kubo, Y. Morikawa, Chem. Lett. (2002) 1078-1079
[14] T. Shido, Y. Iwasawa, J. Catal. 140 (1993) 575-584
[15] W. Jochum, S. Penner, R. Kramer, K. Föttinger, G. Rupprechter, B. Klötzer, J. Catal. 256 (2008) 278-286
[16] C. Jing, J. Hou, Y. Zhang, J. Cryst. Growth 310 (2008) 391-396
[17] V. V. Atuchin, T. A. Gavrilova, S. A. Gromilov, V. G. Kostrovsky, L. D. Pokrovsky, B. Troitskaia, R. S. Vemuri, G. Carbajal-Franco, C. V. Ramana, Cryst. Growth Des. 9 (2008) 1829-1832
[18] H. Kim, S. Shim, J. Lee, Appl. Surf. Sci. 253 (2007) 7207-7210
[19] Q. Zhao, H. Lorenz, O. I. Lebedev, S. Turner, G. Van Tendeloo, B. Klötzer, C.Rameshan, S. Penner, submitted to Appl. Catal. A
[20] F. Izumi, J. Solid State Chem. 38 (1981) 381-385
[21] X. Feng, J. Ma, F. Yang, F. Li, C. Luan, Mat. Lett. 62 (2008) 1809-1811

[22] J. A. Lee, G. V. Raynor, Proc. Phys. Soc., London, 67 (1954) 737-747
[23] V. M. Jimenez, J. P. Espinos, A. R. Gonzalez-Elipe, Surf. Sci. 366 (1996) 556-563
[24] W. E. Boggs, P. S. Trozzo, G. E. Pelissier, J. Electrochem. Soc. 108 (1961) 124-129
[25] L. Sodomka, A. Kleprik, Jemna Mech. Opt. 8 (1963) 43-46
[26] W. Baur, Acta Crystallogr. A 9 (1956) 515-520
[27] M. S. Moreno, R. F. Egerton, J. J. Rehr, P. A. Midgley, Phys. Rev. B 71 (2005) 035103-1 035103-6
[28] [28] R. J. Meyer, Gmelins Handbuch der Anorganischen Chemie, 8. Auflage, 1958, Verlag Chemie, GmbH Weinheim/Bergstrasse
[29] S. Penner, B. Jenewein, H. Gabasch, B. Klötzer, D. Wang, A. Knop-Gericke, R. Schlögl, K. Hayek, J. Catal. 241 (2006) 14-19
[30] Y. Su, X. Liang, S. Li, Y. Chen, Q. Zhou, S. Yin, X. Meng, M. Kong, Mat. Lett. 62 (2008) 1010-1013
[31] M. Ardyanin, H. Rinnert, M. Vergnat, J. Lumin. 129 (2009) 729-733
[32] M. Ardyanin, H. Rinnert, X. Devaux, M. Vergnat, Appl. Phys. Lett. 89 (2006) 011902-1 - 011902-3
[33] N. Jiang, J. Spence, J. Non-Cryst. Solids 353 (2007) 2813-2816